Harnessing high-dimensional hyperentanglement through a biphoton frequency comb

Zhenda Xie[1,2]*, Tian Zhong[3], Sajan Shrestha[2], XinAn Xu[2], Junlin Liang[2], Yan-Xiao Gong[4], Joshua C. Bienfang[5], Alessandro Restelli[5], Jeffrey H. Shapiro[3], Franco N. C. Wong[3] and Chee Wei Wong[1,2]*
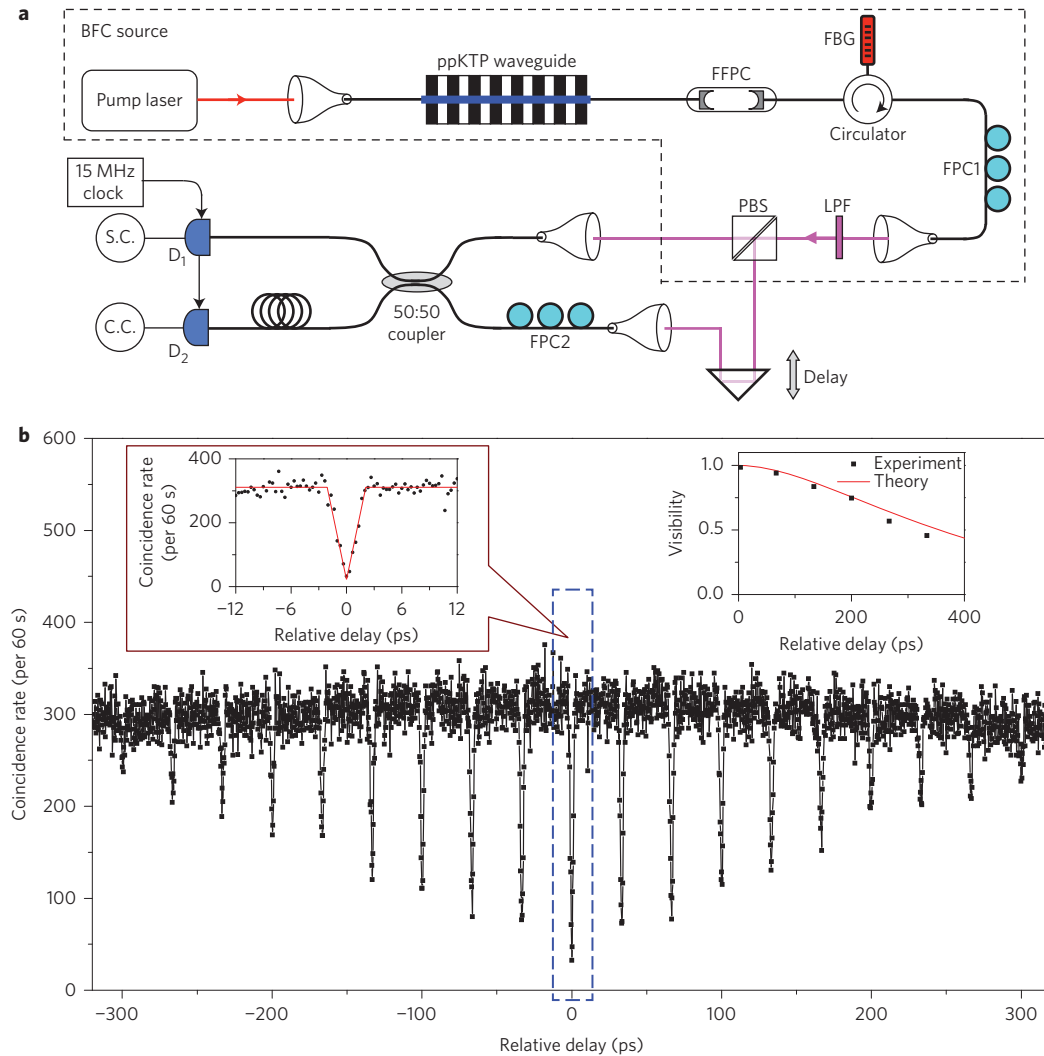
Quantum entanglement is a fundamental resource for secure information processing and communications, and hyperentanglement or high-dimensional entanglement has been separately proposed for its high data capacity and error resilience. The continuous-variable nature of the energy–time entanglement makes it an ideal candidate for efficient high-dimensional coding with minimal limitations. Here, we demonstrate the first simultaneous high-dimensional hyperentanglement using a biphoton frequency comb to harness the full potential in both the energy and time domain. Long-postulated Hong–Ou–Mandel quantum revival is exhibited, with up to 19 time-bins and 96.5% visibilities. We further witness the high-dimensional energy–time entanglement through Franson revivals, observed periodically at integer time-bins, with 97.8% visibility. This qudit state is observed to simultaneously violate the generalized Bell inequality by up to 10.95 standard deviations while observing recurrent Clauser–Horne–Shimony–Holt S-parameters up to 2.76. Our biphoton frequency comb provides a platform for photon-efficient quantum communications towards the ultimate channel capacity through energy–time–polarization high-dimensional encoding.

Increasing the dimensionality of quantum entanglement is a key enabler for high-capacity quantum communications and key distribution[1,2], quantum computation[3] and information processing[4,5], imaging[6] and enhanced quantum phase measurement[7,8]. A large Hilbert space can be achieved through entanglement in more than one degree of freedom (known as hyperentanglement[2,7,9]), where each degree of freedom can also be expanded to more than two dimensions (known as high-dimensional entanglement). The high-dimensional entanglement can be prepared in several physical attributes, for example, in orbital angular momentum[1,10–12] and other spatial modes[13–15]. The drawback of these high-dimensional spatial states is complicated beam-shaping for entanglement generation and detection, which reduces the brightness of the sources as the dimension scales up and complicates their use in optical-fibre-based communications systems. In contrast, the continuous-variable energy–time entanglement[16–22] is intrinsically suitable for high-dimensional coding and, if successful, can potentially be generated and communicated via the telecommunication network. However, most studies focus on time-bin entanglement, which is discrete-variable entanglement with a typical dimensionality of two[23–25]. Difficulties in pump-pulse shaping and phase control limit the dimensionality of the time-bin entanglement[26], and high-dimensional time-bin entanglement has not been fully characterized because of the overwhelmingly complicated analysing interferometers. On the other hand, a biphoton state with a comb-like spectrum could potentially serve for high-dimensional entanglement generation and take full advantage of the continuous-variable energy–time subspace. Based on this state, promising applications have been proposed for quantum computing, secure wavelength-division multiplexing and dense quantum key

distribution[3,27,28]. A phase-coherent biphoton frequency comb (BFC) is also known for its mode-locked behaviour in its second-order correlation. Unlike classical frequency combs, where mode-locking directly relies on phase coherence over individual comb lines, the mode-locked behaviour of a BFC is the representation of the phase coherence of a biphoton wavepacket over comb-line pairs and results in periodic recurrent correlation at different time-bins[29,30]. This time correlation feature can be characterized through quantum interference when passing the BFC through an unbalanced Hong–Ou–Mandel (HOM)-type interferometer[31]. A surprising revival of the correlation dips can be observed at time-bins with half the period of the BFC revival time. However, because of the limited type-I collinear spontaneous parametric downconversion (SPDC) configuration in previous studies[29], post-selection was necessary for BFC generation where the signal and idler photons are indistinguishable, limiting the maximum two-photon interference to 50%.

Here, we achieve high-dimensional hyperentanglement through a BFC. The high-dimensional hyperentanglement of the BFC is fully characterized by four observations. First, the state is prepared at telecommunications wavelengths, without the need for post-selection, by using a type-II high-efficiency periodically-poled KTiOPO₄ (ppKTP) waveguide together with a fibre Fabry–Pérot cavity (FFPC). Because of the type-II phase matching, signal and idler photons can be separated efficiently by a polarizing beamsplitter (PBS), allowing deterministic BFC generation (as first proposed theoretically by one of the authors of ref. 29) to be observed experimentally for the first time. Revival dips with ≈96.5% visibility from two-photon interference in a HOM-type interferometer are observed recurrently, also for the first time, revealing correlation

Figure 1 | Generation and quantum revival observations of the high-dimensional biphoton frequency comb. a, Illustrative experimental scheme. FFPC, fibre Fabry–Pérot cavity; FBG, fibre Bragg grating; FPC, fibre polarization controller; LPF, long-pass filter; PBS, polarizing beamsplitter; P, polarizer; S.C., single counts; C.C., coincidence counts. **b**, Coincidence counting rate as a function of relative delay, ΔT, between the two arms of the HOM interferometer. The HOM revival is observed in the two-photon interference, with dips at 19 time-bins in this case. The visibility change across the different relative delays arises from the single FFPC bandwidth, $\Delta\omega$. The red solid line is the theoretical prediction from the phase-matching bandwidth. Left inset: zoom-in coincidence around zero relative delay between the two arms. The dip width was fit to be 3.86 ± 0.30 ps, which matches well with the 245 GHz phase-matching bandwidth. The measured visibility of the dip is observed at 87.2 ± 1.5, or 96.5% after subtracting the accidental coincidence counts. Right inset: measured bin visibility versus HOM delay, compared with theoretical predictions (Supplementary Section I).

features in the time-bins of the BFC. Second-order frequency correlation and anticorrelation, scanned across the full span of the frequency-bins by narrowband filter pairs, show the good fidelity of the frequency-bin entangled state. Finally, we confirm the generation of high-dimensional energy–time entanglement using a Franson interferometer, which can be regarded as a generalized Bell inequality test. For the first time, Franson interference fringes are observed to revive periodically at different time-bin intervals with visibilities up to 97.8%. Based on these three measurements, we encode extra qubits in the BFC photon pairs by mixing them on a 50:50 fibre beamsplitter (FBS). We witness the hyperentanglement by simultaneous polarization and Franson interferometer analysis, demonstrating a generalized Bell inequality in two polarization and four time-bin subspaces up to 10.95 and 8.34 standard deviations (s.d.) respectively. The Clauser–Horne–Shimony–Holt (CHSH) S-parameters are determined for the polarization basis across the different time-bins with a maximum up to 2.76.

Figure 1a presents the experimental scheme. The SPDC entangled photon pairs are generated by a high-efficiency type-II ppKTP waveguide, described in detail in ref. 32. The frequency-degenerate SPDC phase matching is designed for a 1,316 nm output with a bandwidth of ≈245 GHz. The type-II BFC is generated by passing the SPDC photons through a FFPC (Micron Optics; note that the identification of any commercial product or trade name does not imply endorsement or recommendation by the National Institute of Standards and Technology), with the signal and idler photons in orthogonal polarizations (H, horizontal; V, vertical). A BFC state is expressed as

$$|\psi\rangle = \sum_{m=-N}^{N} \int d\Omega f(\Omega - m\Delta\Omega)\hat{a}_H^\dagger(\omega_p/2 + \Omega)\hat{a}_V^\dagger(\omega_p/2 - \Omega)|0\rangle \quad (1)$$

where $\Delta\Omega$ is the spacing between the frequency bins (that is, the free spectral range of the FFPC in rad s^{-1}, Ω is the detuning of the SPDC
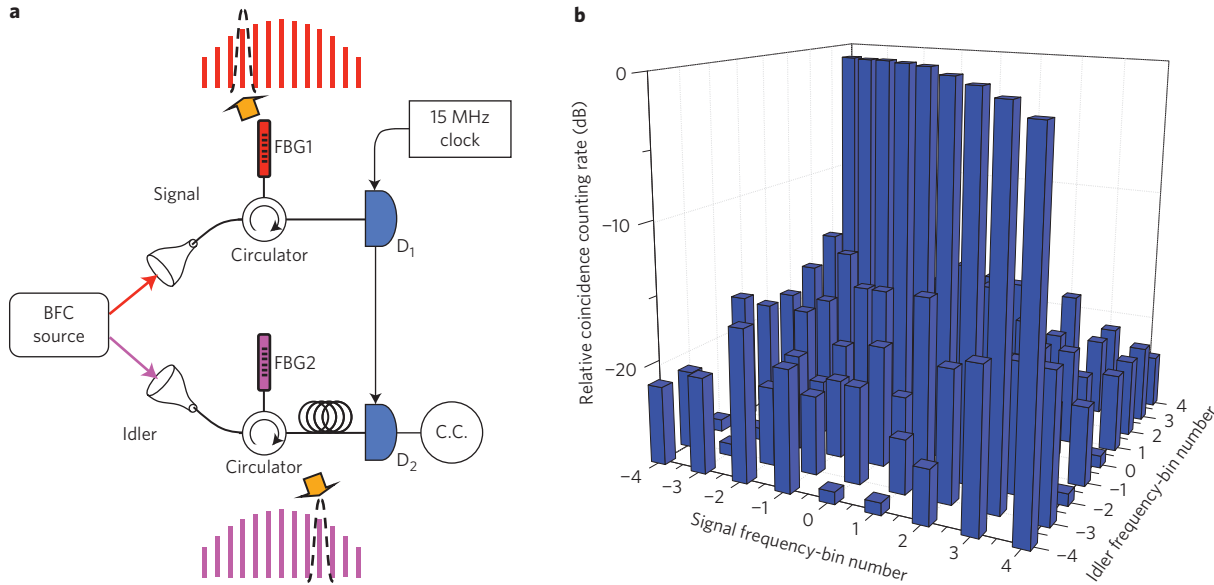
Figure 2 | Quantum frequency correlation measurement of the biphoton frequency comb. a, Experimental schematic for the frequency correlation measurement. Signal and idler photons are sent to two narrowband filters for the frequency bin correlation measurement with coincidence counting. Each filter consists of a FBG and a circulator. The FBGs have a matched FWHM bandwidth of 100 pm and are thermally tuned for scans from the −4th to +4th frequency bins from the centre. **b**, Measured frequency correlation of the BFC. The relative coincidence counting rate is recorded while the signal and idler filters are set at different frequency-bin numbers.

biphotons from their central frequency, and the state's spectral amplitude $f(\Omega - m\Delta\Omega)$ is the single frequency-bin profile, defined by the Lorentzian-shape transmission of the FFPC with a full-width at half-maximum (FWHM) of $2\Delta\omega$, and

$$f(\Omega) = \frac{1}{[(\Delta\omega)^2 + \Omega^2]} \quad (2)$$

The signal and idler photons are separated with 100% probability by a polarizing beamsplitter or, in other words, the BFC is thus prepared without post-selection. The temporal wavefunction of the BFC can be written as

$$|\psi_t\rangle = \int d\tau \exp(-\Delta\omega|\tau|) \frac{\sin[(2N+1)\Delta\Omega\tau/2]}{\sin(\Delta\Omega\tau/2)} \hat{a}_H^\dagger(t)\hat{a}_V^\dagger(t+\tau)|0\rangle \quad (3)$$

where the exponential decay is slowly varying because of small $\Delta\omega$ and thus the temporal behaviour of the BFC is mainly determined by the term $(\sin[(2N+1)\Delta\Omega\tau/2]/\sin(\Delta\Omega\tau/2))$, with a repetition time of $T = 2\pi/\Delta\Omega$.

The FFPC has a free spectral range (FSR) and bandwidth of 15.15 GHz and 1.36 GHz, respectively. The repetition period T of the BFC is ≈66.2 ps. The FFPC is mounted onto a thermoelectric cooling sub-assembly with minimized stress to eliminate polarization birefringence and with ≈1 mK high-performance temperature control. From our measurements, there is no observable polarization birefringence in the FFPC, so the signal and idler photons have the same spectrum after they pass through the cavity. Due to the type-II configuration, there is no probability that both photons propagate in the same arm of the HOM interferometer; this configuration yields a potential maximum of 100% visibility of the two-photon interference.

The pump is a Fabry–Pérot laser diode that is stabilized with self-injection-locking through double-pass first-order-diffraction feedback using an external grating (for details see Supplementary Section IV and Methods). It is passively stabilized with modest low-noise current and temperature control for single-longitudinal-mode lasing at 658 nm, with a stability of less than 2 MHz within 200 s (measured with the Franson interference experiment; Supplementary Section IV). We first match the FFPC wavelength with the pump via temperature tuning and second harmonic generation (SHG) from a frequency-stabilized distributed feedback (DFB) reference laser at 1,316 nm. The SHG is monitored with a wavemeter (WS-7, HighFinesse) to 60 MHz accuracy, allowing the tuning of the laser diode current and first-order-feedback diffraction angle to match the FFPC for BFC generation. The BFC spectrum is further cleaned by a fibre Bragg grating (FBG) with a circulator and a free-space long-pass filter that blocks residual pump light. The FBG is chosen to have a bandwidth of 346 GHz, larger than the 245 GHz phase-matching bandwidth, and is simultaneously temperature-controlled to match the central wavelength of the SPDC. A polarizing beamsplitter separates the orthogonally polarized signal and idler photons.

We first characterize the mode-locked behaviour using a HOM interferometer. The signal and idler photons are sent through different arms of the interferometer. A fibre polarization controller in the interferometer's lower arm controls the idler photon polarization, so that the two photons have the same polarization at the FBS. An optical delay line consisting of a prism and a motorized long-travel linear stage (DDS220, Thorlabs) is used to change the relative timing delay between the two arms of the HOM interferometer. The position-dependent insertion loss of the optical delay line is measured to be less than 0.02 dB throughout its entire travel range of 220 mm. The coincidence measurements are performed with two InGaAs single-photon detectors D_1 (≈20% detection efficiency and 1 ns gate width) and D_2 (≈25% detection efficiency and 3 ns gate width). D_1 is triggered at 15 MHz, and its output signal is used to trigger D_2. As a result, coincidences can be detected directly from the D_2 counting rate if the proper optical delay is applied to compensate for the electronic delay. Taking into account the waveguide-to-fibre coupling and transmission efficiencies of the optical components, the overall signal and idler detection efficiencies are estimated to be $\eta_s = 0.92\%$ and $\eta_i = 1.14\%$, respectively. Figure 1b shows the experimental results obtained by scanning the optical
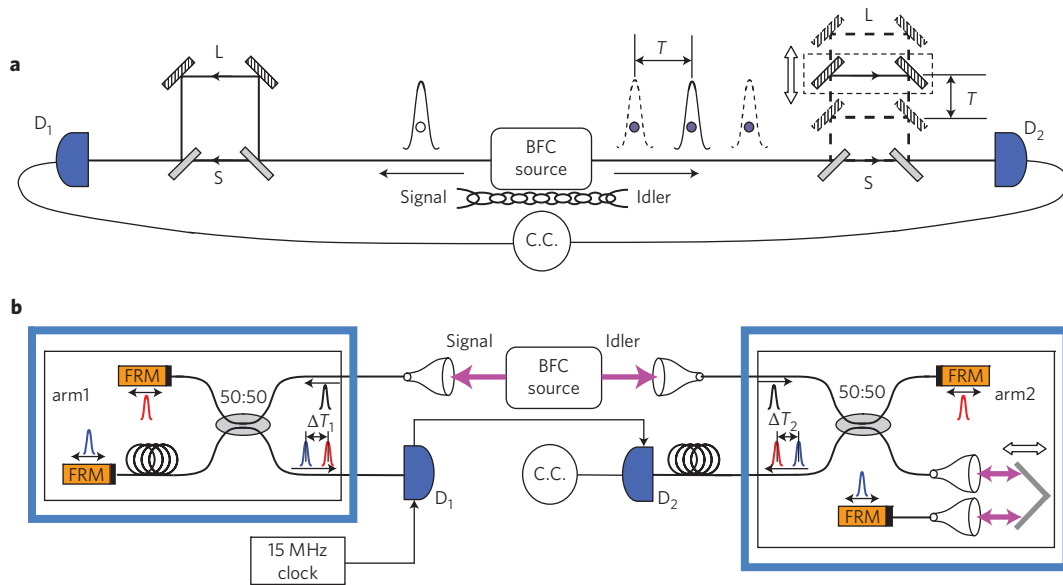
Figure 3 | Franson interference of the high-dimensional biphoton frequency comb. a, Schematic map and concept of Franson interference of the BFC. The BFC is prepared with high-dimensional correlation features of mode-locked behaviour with a repetition period of T. Franson-type interference between the long–long (L–L) and short–short (S–S) events can therefore be observed when $\Delta T = NT$, where N is an integer. **b**, Experimental Franson interference set-up. Faraday mirrors (FRMs) are used to compensate the stress-induced birefringence of the single-mode fibre interferometers. A compact optical delay line was used in the longer path of arm2 to achieve different imbalances ΔT (= $\Delta T_2 - \Delta T_1$). Both arms are double-temperature stabilized, first on the custom aluminium plate mountings and second by the sealed enclosures (light blue thick lines).

delay between the two arms of the HOM interferometer from −320 ps to 320 ps, with a pump power of 2 mW. At this power level the generation rate is ≈3.3×10^{-3} pairs per gate, and multi-pair events can be neglected. We obtain revival dips for the coincidence counting rate R_{12} at the two outputs of the HOM interferometer (single-photon rates are shown in Supplementary Section V). The spacing between the dips is 33.4 ps, which matches half the repetition period of the BFC, and agrees with our theory and numerical modelling (see Supplementary Section I for details). We also note that our earlier analysis[30] involved a movable beamsplitter for both beams (for a T recurrence), but in the present measurement set-up only the idler beam is delayed (for a $T/2$ recurrence), supported by the same type of analysis and physical interpretation. The visibility of the dips decreases exponentially (right inset in Fig. 1b) due to the Lorentzian lineshape spectra of the SPDC individual photons after they pass through the FFPC. A zoom-in of the dip around the zero delay point is shown in the left inset of Fig. 1b. The maximum visibility is measured to be 87.2 ± 1.5, or 96.5% after subtracting the accidental coincidence counts (≈17.3 per 70 s). Its base-to-base width is fitted to be 3.86 ± 0.30 ps, corresponding to a two-photon bandwidth of 259 ± 20 GHz, which agrees with the expected 245 GHz phase-matching bandwidth. More details are provided in Supplementary Section V. Considering the measured bin spacing $\Delta\Omega/2\pi$ of 14.98 GHz, 17 frequency-bins are generated in our measurements within the phase-matching bandwidth, equivalent to ≈4 quantum bits per photon for high-dimensional frequency entanglement.

To test the purity of the high-dimensional frequency-bin entanglement, we further measure the correlation between different frequency-bins for the signal and idler photons. Each pair of frequency-bins is filtered out by a set of narrowband filters for the signal and idler photons. As shown in Fig. 2, each filter is composed of a FBG centred at 1,316 nm with 100 pm FWHM and an optical circulator. Both FBGs are embedded in a custom-built temperature-controlled housing for fine spectral tuning. The coincidence counting rate is recorded while the filters are set at different combinations of the signal–idler frequency-bin basis. The tuning range is bounded by

the maximum tuned FBG temperature (currently up to ≈100 °C), and in this case nine frequency-bins can be examined for the signal and idler biphoton. We number these bins #−4 to #4, with #0 indicating the central bin, as shown in Fig. 2b. We see that high coincidence counting rates are measured only when the filters are set at the corresponding positive–negative frequency-bins, according to equation (1). The suppression ratio between the corresponding and non-corresponding counting rate exceeds 13.8 dB for adjacent bins (including ≈2% leakage from the bandpass filters), or 16.6 dB for non-adjacent bins. We note that, through conjugate state projection[20], observation of both the HOM recurrence and frequency correlation supports the entangled nature of the BFC.

To further characterize the energy–time entanglement of the BFC, we built an interferometer to examine Franson interference, as shown schematically in Fig. 3a. The Franson interferometer[16,33] comprises two unbalanced Mach–Zehnder interferometers (for details see Supplementary Methods and Supplementary Section III), with imbalances ΔT_1 and ΔT_2. Usually, Franson interference arises from two indistinguishable two-photon events: both signal and idler photons take the long arm (L–L) and both photons take the short arm (S–S). This interference only happens when $\Delta T \equiv \Delta T_1 - \Delta T_2 = 0$ to within the single photon coherence length, which is 1.81 ps in our case. Because of the high-dimensional frequency entanglement, however, Franson interference can be observed at different time revivals. As discussed before, the BFC features a mode-locked revival in temporal correlation, with a repetition period of T. Such Franson interference revival can therefore be observed for integer temporal delays $\Delta T = NT$, where N is an integer (including 0). Detailed theory and modelling are provided in Supplementary Section II for the revival of the Franson interference, and the experimental set-up is shown in Fig. 3b. The signal and idler photons are sent to two fibre-based interferometers (arm1 and arm2) with imbalances ΔT_1 and ΔT_2, respectively. Details on the pump laser and interferometer set-up stabilisation are described in Supplementary Sections III and IV and in the Methods. Each arm includes double-pass temperature-stabilized
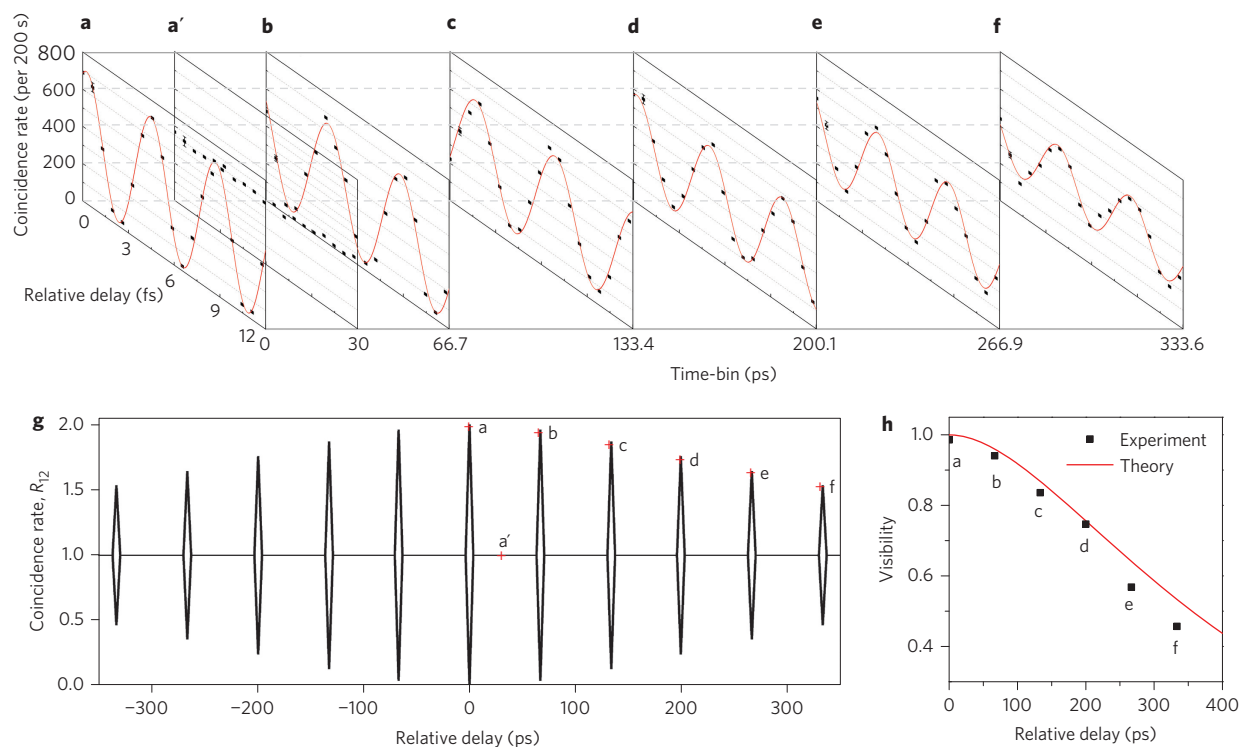
Figure 4 | Measured Franson interference around different relative delays of arm2. a–f, Franson interferences at time-bins #0 ($\Delta T = 0$), #1 ($\Delta T = 66.7$ ps), #2 ($\Delta T = 133.4$ ps), #3 ($\Delta T = 200.1$ ps), #4 ($\Delta T = 266.9$ ps) and #5 ($\Delta T = 333.6$ ps), respectively. Also included in **a′** is the interference measured away from the above time-bins at $\Delta T = 30$ ps, with no observable interference fringes. The data points in each panel (of the different relative Franson delays) include the measured error bars across each data set, arising from Poisson statistics, experimental drift and measurement noise. The error bars from repeated coincidence measurements are much smaller than the observed coincidence rates in our measurement and set-up. In each panel, the red line denotes the numerical modelling of the Franson interference on the high-dimensional quantum state. **g,** Theoretical fringe envelope of Franson interference for the high-dimensional biphoton frequency comb, with superimposed experimental observations. The marked labels (**a–f,a′**) correspond to the actual delay points from which the above measurements were taken. **h,** Witnessed visibility of high-dimensional Franson interference fringes as a function of ΔT. The experimental (and theoretical) witnessed visibilities for the kth-order peaks are 97.8 (100), 93.3 (96.0), 83.0 (86.8), 74.1 (75.6), 59.0 (64.0) and 45.4% (53.3%), respectively.

Michelson interferometers, and two of the output ports of the fibre 50:50 beamsplitter are spliced onto two Faraday mirrors, with single photons being collected from the reflection. They therefore effectively work as a Mach–Zehnder interferometer, and the polarization instability inside the fibres is self-compensated accurately. Following the general requirement for Franson interference, the ΔT_1 and ΔT_2 time differences (5 ns in our set-up) are tuned to be much larger than the single-photon coherence time and the timing jitter of the single-photon detectors. The relative timing between the single-photon detection gates is programmed such that events are only recorded for the L–L and S–S events. Both arms are mounted on aluminium housings with $\approx$1 mK temperature control accuracy. Enclosures are further used to seal the interferometers with additional temperature control for isolating mechanical and thermal shocks. To detect the Franson interference at different temporal revivals, we include a free-space delay line on arm2, which gives us the capability to study the Franson interference with possible detuning ΔT up to 360 ps, bounded by the free-space delay line travel and for up to six positive-delay time-bins.

We are interested here in the regime of $\Delta T \geq 0$, because of the symmetry of the signal and idler. In particular, this allows us to examine the interference visibility over a larger time frame, for the same stage travel range. With ΔT_2 fixed at each point, the phase-sensitive interference is achieved by fine control of the arm1 temperature, which tunes ΔT_1. As shown in Fig. 4, the revival of Franson interference is only observed exactly at the periodic time-bins $\Delta T = NT$, whereas no interference is observed for other ΔT values

between these bins. The period of the revival time bins is 66.7 ps, which corresponds exactly to the round-trip time of the FFPC ($2\pi/\Delta\Omega$). The visibilities of the interference fringes are measured to be 94.2, 89.3, 79.7, 71.1, 51.0 and 43.6%, or, after subtracting the accidental coincidence counts, 97.8, 93.3, 83.0, 74.1, 59.0 and 45.4%, respectively. The visibility decreases because of the non-zero linewidth of each frequency bin and is captured in our theory (Supplementary Section II). We understand this as a generalized Bell inequality violation for a high-dimensional state at four time-bins from the centre. We only measured for $\Delta T \geq 0$, but could expect the violation of the generalized Bell inequality at the other three inverse symmetric time bins of ΔT at -66.7 ps, -133.4 ps and -200.1 ps, based on symmetry with the three positive time-bins observed.

Figure 5 shows the high-dimensional hyperentanglement by mixing the signal and idler photons on a 50:50 FBS (for details see Supplementary Section VI). In the experiment, hyperentanglement is generated based on the HOM-interference set-up fixed at the central dip, but with polarization adjusted so that the signal and idler photons are orthogonally polarized at the FBS for hyperentanglement generation. Two polarizers P_1 and P_2 are used for the polarization analysis, which is cascaded with the Franson interferometer for the energy–time entanglement measurement at the same time. One set of half and quarter waveplates are placed before each polarizer to compensate the polarization change in the fibre after the FBS. An additional thick multi-order full waveplate is used in the lower arm, which can be twisted along its

5
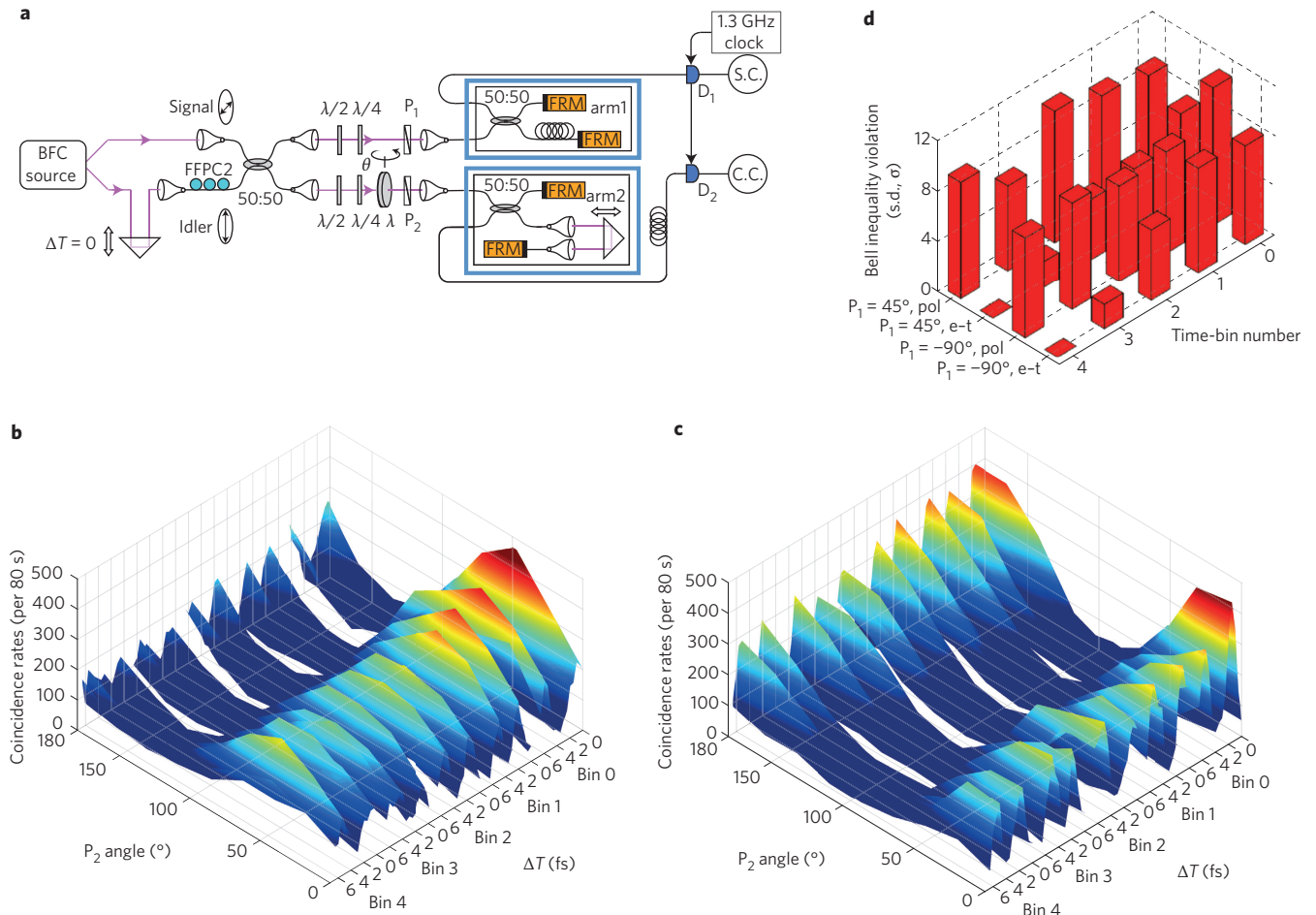
Figure 5 | High-dimensional hyperentanglement on polarization and energy–time basis. a, Set-up for the high-dimensional two degree-of-freedom entanglement measurement. The state is generated by mixing the signal and idler photons at the 50:50 fibre beamsplitter with orthogonal polarizations. Perfect temporal overlap between signal and idler photons is ensured by the HOM interference, as already discussed. High-dimensional hyperentanglement is measured with polarization analysis using polarizers P_1 and P_2, cascaded with a Franson interferometer. $\lambda/2$, half waveplate; $\lambda/4$, quarter waveplate; λ, multi-order full waveplate. **b,c**, Measured two-photon interference fringes when P_1 is set at 45 and 90 degrees, respectively. The period variance of the fringe on the temporal domain arises because of a slow pump laser drift. **d**, Measured Bell inequality violation at different time-bins and P_1 angles. pol, polarization basis; e–t, energy–time basis.

fast axis (fixed in the horizontal plane) to change the phase delay between the horizontally and vertically polarized light. Therefore, we successfully generated the following high-dimensional hyperentangled state when a coincidence is measured:

$$|\psi'\rangle = \sum_{m=-N}^{N} \int d\Omega f(\Omega - m\Delta\Omega) \times (|H, \omega_{\mathrm{p}}/2 + \Omega\rangle_1 |V, \omega_{\mathrm{p}}/2 - \Omega\rangle_2$$
$$+ |V, \omega_{\mathrm{p}}/2 + \Omega\rangle_1 |H, \omega_{\mathrm{p}}/2 - \Omega\rangle_2) \quad (4)$$

Such hyperentanglement is tested using coincidence measurement by scanning P_2 and the Franson interferometer while P1 is set at 45° or 90° and ΔT is fixed at time-bins #0 to #5. A 1.3 GHz self-differencing InGaAs single-photon detector[34,35] is used as D_1 to maximize the gated detection rate. As shown in Fig. 5b,c, clear interference fringes were obtained over both the polarization and energy–time basis, with visibilities up to 96.7 and 95.9%, respectively, after dark count subtraction of a 0.44 s^{-1} rate. Analysed within the two polarization and four time-bin subspaces, this corresponds to Bell violation up to 10.95 and 8.34 s.d., respectively. The CHSH S-parameter is observed for the polarization basis up to $S = 2.76$; details on the photon statistics are presented in Fig. 5d and listed in Supplementary Section VII, Table 1.

In summary, we have demonstrated a high-dimensional hyperentanglement of polarization and energy–time subspaces using a BFC. Based on continuous-variable energy–time entanglement, unlimited qubits can be coded on the BFC by increasing the number of comb line pairs with a plane wave pump. Here, we show an example of bright BFC generation with 5 qubits per photon, from a type-II SPDC process in a ppKTP waveguide without post-selection. Nineteen HOM dip recurrences with a maximum visibility of 96.5% are observed in a stabilized interferometer. High-dimensional energy–time entanglement is proven by Franson interference, which can be considered as a generalized Bell inequality test. Revival of the Franson interference has been witnessed at periodic time-bins, where the time-bin separation is the cavity round-trip time, that is, the revival time of the BFC. The interference visibility was measured up to 97.8%. The generalized Bell inequality was violated in four out of six measured time-bins, or seven time-bins in total considering the symmetry. High-dimensional hyperentanglement was further generated and characterized with high fidelity in both polarization and energy–time subspaces, with Bell inequality violations up to 10.95 and 8.34 s.d. respectively, with measured polarization CHSH S-parameters up to 2.76. It should be noted that the generation rate of the entangled biphoton frequency comb from our high-performance ppKTP waveguide

exceeds 72.2 pairs s^{-1} MHz^{-1} mW^{-1}, taking into account all detection losses and the 1.5% duty cycle for the detection time, which is higher than that of cavity-enhanced SPDC using bulk crystals. If the propagation loss of the ppKTP waveguide can be further reduced, the waveguide can be located inside an optical cavity and the brightness of the BFC further enhanced. Such a bright high-dimensional hyperentangled BFC can encode multiple qubits onto a single photon pair without losing the high photon flux and thus further increase the photon efficiency, with applications in dense quantum information processing and secure quantum key distribution channels.

Methods

Methods and any associated references are available in the online version of the paper.

References

1. Dada, A. C., Leach, J., Buller, G. S., Padgett, M. J. & Andersson, E. Experimental high-dimensional two-photon entanglement and violations of generalized Bell inequalities. *Nature Phys.* **7,** 677–680 (2011).
2. Barreiro, J. T., Wei, T. C. & Kwiat, P. G. Beating the channel capacity of linear photonic superdense coding. *Nature Phys.* **4,** 282–286 (2008).
3. Menicucci, N. C., Flammia, S. T. & Pfister, O. One-way quantum computing in the optical frequency comb. *Phys. Rev. Lett.* **101,** 130501 (2008).
4. Krenn, M. *et al.* Generation and confirmation of a (100 × 100)-dimensional entangled quantum system. *Proc. Natl Acad. Sci. USA* **111,** 6243–6247 (2014).
5. Strobel, H. *et al.* Fisher information and entanglement of non-Gaussian spin states. *Science* **345,** 424–427 (2014).
6. Howland, G. A. & Howell, J. C. Efficient high-dimensional entanglement imaging with a compressive-sensing double-pixel camera. *Phys. Rev. X* **3,** 011013 (2013).
7. Bao, W.-B. *et al.* Experimental demonstration of a hyper-entangled ten-qubit Schrödinger cat state. *Nature Phys.* **6,** 331–335 (2010).
8. Sun, F. W. *et al.* Experimental demonstration of phase measurement precision beating standard quantum limit by projection measurement. *Europhys. Lett.* **82,** 24001 (2008).
9. Badziag, P., Brukner, C., Laskowski, W., Pterek, T. & Zukowski, M. Experimentally friendly geometrical criteria for entanglement. *Phys. Rev. Lett.* **100,** 140403 (2008).
10. Fickler, R. *et al.* Quantum entanglement of high angular momenta. *Science* **338,** 640–643 (2012).
11. Fickler, R. *et al.* Interface between path and orbital angular momentum entanglement for high-dimensional photonic quantum information. *Nature Commun.* **5,** 4502 (2014).
12. Leach, J. *et al.* Quantum correlations in optical angle–orbital angular momentum variables. *Science* **329,** 662–665 (2010).
13. Peruzzo, A. *et al.* Quantum walks of correlated photons. *Science* **329,** 1500–1503 (2010).
14. Edgar, M. P. *et al.* Imaging high-dimensional spatial entanglement with a camera. *Nature Commun.* **3,** 984 (2012).
15. Dixon, P. B., Howland, G. A., Schneeloch, J. & Howell, J. C. Quantum mutual information capacity for high-dimensional entangled states. *Phys. Rev. Lett.* **108,** 143603 (2012).
16. Franson, J. D. Bell inequality for position and time. *Phys. Rev. Lett.* **62,** 2205–2208 (1989).
17. Shalm, L. K. *et al.* Three-photon energy–time entanglement. *Nature Phys.* **9,** 19–22 (2013).
18. Cuevas, A. *et al.* Long-distance distribution of genuine energy–time entanglement. *Nature Commun.* **4,** 2871 (2013).
19. Thew, R. T., Acin, A., Zbinden, H. & Gisin, N. Bell-type test of energy–time entangled qutrits. *Phys. Rev. Lett.* **93,** 010503 (2004).
20. Lloyd, S., Shapiro, J. H. & Wong, F. N. C. Quantum magic bullets by means of entanglement. *J. Opt. Soc. Am. B* **19,** 312–318 (2002).
21. Ali-Khan, I., Broadbent, C. J. & Howell, J. C. Large-alphabet quantum key distribution using energy–time entangled bipartite states. *Phys. Rev. Lett.* **98,** 060503 (2007).
22. Zhong, T. *et al.* Photon-efficient quantum key distribution using time–energy entanglement with high-dimensional encoding. *New J. Phys.* **17,** 022002 (2015).
23. Takeda, S., Mizuta, T., Fuwa, M., van Loock, P. & Furusawa, A. Deterministic quantum teleportation of photonic quantum bits by a hybrid technique. *Nature* **500,** 315–318 (2013).
24. Jayakumar, H. *et al.* Time-bin entangled photons from a quantum dot. *Nature Commun.* **5,** 4251 (2014).
25. Marcikic, I. *et al.* Time-bin entangled qubits for quantum communication created by femtosecond pulses. *Phys. Rev. A* **66,** 062308 (2002).
26. De Riedmatten, H. *et al.* Tailoring photonic entanglement in high-dimensional Hilbert spaces. *Phys. Rev. A* **69,** 050304(R) (2004).
27. Roslund, J., de Araújo, R. M., Jiang, S., Fabre, C. & Treps, N. Wavelength-multiplexed quantum networks with ultrafast frequency combs. *Nature Photon.* **8,** 109–112 (2014).
28. Pinel, O. *et al.* Generation and characterization of multimode quantum frequency combs. *Phys. Rev. Lett.* **108,** 083601 (2012).
29. Lu, Y. J., Campbell, R. L. & Ou, Z. Y. Mode-locked two-photon states. *Phys. Rev. Lett.* **91,** 163602 (2003).
30. Shapiro, J. H. Coincidence dips and revivals from a Type-II optical parametric amplifier. *Technical Digest of Topical Conference on Nonlinear Optics*, paper FC7-1, Maui, HI, 2002.
31. Hong, C. K., Ou, Z. Y. & Mandel, L. Measurement of subpicosecond time intervals between two photons by interference. *Phys. Rev. Lett.* **59,** 2044–2046 (1987).
32. Zhong, T., Wong, F. N. C., Roberts, T. D. & Battle, P. High performance photon-pair source based on a fiber-coupled periodically poled KTiOPO$_4$ waveguide. *Opt. Express* **17,** 12019–12030 (2009).
33. Gisin, N. & Thew, R. Quantum communication. *Nature Photon.* **1,** 165–171 (2007).
34. Restelli, A. & Bienfang, J. C. Avalanche discrimination and high-speed counting in periodically gated single-photon avalanche diodes. *Proc. SPIE.* **8375,** 83750Z (2012).
35. Yuan, Z. L., Kardynal, B. E., Sharpe, A. W. & Shields, A. J. High speed single photon detection in the near infrared. *Appl. Phys. Lett.* **91,** 041114 (2007).

Author contributions

Z.X., T.Z., S.S., X.X. and J.L. performed the measurements. J.C.B. and A.R. developed the 1.3 GHz detectors. T.Z., Y.X.G., F.N.C.W. and J.H.S. provided the theory and samples. All authors helped with manuscript preparation.

Additional information

Supplementary information is available in the online version of the paper. Reprints and permissions information is available online at www.nature.com/reprints. Correspondence and requests for materials should be addressed to Z.X. and C.W.W.

Competing financial interests

The authors declare no competing financial interests.

Methods

Stabilized self-injection-locked 658 nm pump laser. For the Franson measurements, good long- and short-term stability of the 658 nm pump laser is required, as this stability defines the coherence time of the two-photon state. This coherence time should be much longer than the path length difference ($\approx$5 ns in our Franson measurements). We therefore designed and built a laser stabilized through self-injection-locking, in a configuration similar to the Littman–Metcalf cavity. With its single spatial mode, the longitudinal modes are selected through a diffraction grating (first order back into the diode; zeroth order as output) with an achieved mode-rejection ratio of more than 30 dB. Three temperature controllers are used to stabilize the doubly-enclosed laser system and a low-noise controller from Vescent Photonics (D2-105) drives the laser diode. With this design, a 2 MHz stability is achieved for 200 s measurement and integration timescales, as confirmed with the Franson interferometer. For longer timescales (12 h), a wavelength meter indicates $\approx$100 MHz drift. More details on the characterization, set-up and design are provided in Supplementary Section IV.

Franson interferometer. For the long-term phase-sensitive interference measurements, the fibre-based Franson interference needs to be carefully stabilized. Both interferometer arms are double-enclosed and sealed, and temperature-controlled with Peltier modules. Closed-loop piezoelectric control fine-tunes the arm2 delay. We designed and custom-built a pair of fibre collimators for fine focal adjustment, coupling and alignment. The double-pass delay line insertion loss is less than 0.4 ± 0.05 dB over the entire 27 mm delay-travel range (up to 360 ps in the reflected double-pass configuration). To verify the Franson interferometer stability, arm1 and arm2 are connected in series, and the interference visibility is observed up to $49.8 \pm 1.0\%$ for both short and long term, near or right at the 50% classical limit. The delay-temperature tuning transduction is quantified at 127 as per mK. More details on the characterization, set-up and design are provided in Supplementary Section III.